remote sensing

MDPI

Article

A Hybrid Model for Mapping Relative Differences in Belowground Biomass and Root:Shoot Ratios Using Spectral Reflectance, Foliar N and Plant Biophysical Data within Coastal Marsh

Jessica L. O'Connell [1,2,*], Kristin B. Byrd [3] and Maggi Kelly [1]

Received: 27 July 2015; Accepted: 25 November 2015; Published: 5 December 2015
Academic Editors: Richard W. Gould, Jr., Yoshio Inoue and Prasad S. Thenkabail

[1] Department of Environmental Sciences Policy and Management, University of California, Berkeley, Berkeley, CA 94720, USA; maggi@berkeley.edu
[2] Department of Marine Sciences, University of Georgia, Athens, GA 30602, USA
[3] U.S. Geological Survey, Western Geographic Science Center, Menlo Park, CA 94025, USA; kbyrd@usgs.gov
* Correspondence: jessica.oconnell@okstate.edu; Tel.: +1-510-642-7272

Abstract: Broad-scale estimates of belowground biomass are needed to understand wetland resiliency and C and N cycling, but these estimates are difficult to obtain because root:shoot ratios vary considerably both within and between species. We used remotely-sensed estimates of two aboveground plant characteristics, aboveground biomass and % foliar N to explore biomass allocation in low diversity freshwater impounded peatlands (Sacramento-San Joaquin River Delta, CA, USA). We developed a hybrid modeling approach to relate remotely-sensed estimates of % foliar N (a surrogate for environmental N and plant available nutrients) and aboveground biomass to field-measured belowground biomass for species specific and mixed species models. We estimated up to 90% of variation in foliar N concentration using partial least squares (PLS) regression of full-spectrum field spectrometer reflectance data. Landsat 7 reflectance data explained up to 70% of % foliar N and 67% of aboveground biomass. Spectrally estimated foliar N or aboveground biomass had negative relationships with belowground biomass and root:shoot ratio in both *Schoenoplectus acutus* and *Typha,* consistent with a balanced growth model, which suggests plants only allocate growth belowground when additional nutrients are necessary to support shoot development. Hybrid models explained up to 76% of variation in belowground biomass and 86% of variation in root:shoot ratio. Our modeling approach provides a method for developing maps of spatial variation in wetland belowground biomass.

Keywords*:* belowground biomass; carbon cycling; coastal tidal freshwater wetlands; eutrophication; Landsat; nitrogen cycling; productivity; root:shoot ratio; remote-sensing; sea level rise

1. Background and Rationale

Remote-sensing models of aboveground biomass are commonly derived from optical data [1,2], however monitoring belowground biomass and root:shoot ratios to understand whole plant production patterns remains challenging. Understanding dynamics in belowground biomass is important because roots and rhizomes are the precursors and dominant components of soil organic carbon [3]. Soil organic carbon represents more than two-thirds of terrestrial organic carbon, significantly more carbon than found in terrestrial vegetation, and has soil residence times exceeding thousands of years [4]. In this paper, we present a hybrid modeling approach for scaling up field measured point estimates of belowground biomass and root:shoot ratios using remote-sensing and linear modeling. We compare mixed species and species specific models and quantify prediction error.

Our model system was emergent vegetation within coastal freshwater marsh. We selected this system because there is an urgent need to understand dynamics regulating belowground biomass within coastal wetlands. Wetland belowground biomass is the precursor to peat, a form of stabilized belowground organic matter mostly of vegetation root origin [5]. Peat up to 15 m deep, a substantial carbon pool, has been observed in some coastal freshwater wetlands [6], and is higher than in most other natural ecosystems, representing 16%–33% of the global soil carbon pool [7]. The combination of sea level rise, saltwater intrusion, peat collapse and subsidence of coastal marsh surface elevation may result in substantial global wetland losses [8–11]. However, accretion of belowground organic matter adds to surface elevation within wetlands, alleviating flooding as sea levels rise, and contributing to long-term ecosystem sustainability [12–14]. Coastal marshes are important sites of wildlife habitat, water storage and purification, and other ecosystem services [15]. Therefore, preservation of coastal marsh is an essential conservation goal, and an important first step involves understanding belowground biomass dynamics across landscapes.

To estimate belowground biomass, we used remote-sensing approaches. Remote-sensing of vegetation within wetlands has a long tradition [16]. For example, multispectral sensors have been used within wetlands to classify vegetation, map habitats, and estimate aboveground biomass [17–19]. In particular Landsat satellite data, with 16 d return frequency, provides the opportunity to capture seasonal trends across growing seasons, aiding development of robust models of plant characteristics [20–22]. Hyperspectral sensors have advantages over multispectral sensors for wetland studies because narrow bands allow improved discrimination of vegetation signals from background noise [17,23]. However hyperspectral sensors have trade-offs because they generally have high acquisition cost, low return frequency, or coarse to moderate spatial resolution [23]. Selecting sensors for wetland remote-sensing applications requires matching sensor strengths and limitations to study goals [21].

Remote-sensing of wetlands has special challenges [17,24]. Wetlands are transitional between terrestrial and aquatic habitats and can have high spatial and temporal pixel heterogeneity [25,26]. Cover types within wetlands include dense emergent vegetation, and also background cover of shallow water, submerged aquatic vegetation, mud substrate, and dead vegetation. Such background effects commonly reduce the predictive value of spectral reflectance signals in emergent wetlands [20]. Near infrared wavelengths in particular are attenuated by open water in pixel backgrounds, making direct application of normalized difference vegetation index (NDVI) type indices to wetland vegetation challenging [27,28].

To overcome challenges of wetland remote-sensing, we used an analytical approach designed to take advantage of the complete spectral information measured by remote-sensing platforms: partial least squares (PLS) regression. PLS regression, a full spectrum multivariate method, maximizes explained variance among plant responses and spectral reflectance signals [29,30]. PLS uses an Eigen-vector based approach to reduce many multicolinear predictors, such as spectral data, to a few independent components. These components maximize predictive value and minimize background effects introduced by non-target cover types such as water and dead vegetation [31].

Generating remote-sensing models of belowground plant characteristics requires identifying aboveground proxies that can be measured with remote-sensing tools. While wide fluctuations in above *vs.* belowground growth exist within and among species [32], aboveground plant characteristics may be related to belowground biomass and root:shoot ratios according to ecological theories of plant growth. For example, foliar N often has been associated with belowground growth rates [33–35]. Foliar N may be a good indicator of long-term plant available nutrients because it reflects average nutrients absorbed by plants from water and sediments over time [36–40]. One hypothesis relating belowground growth to nutrient availability is the balanced growth model, sometimes called "optimal partitioning" [41,42], which suggests plants allocate growth toward growth limiting resources. In this view, new growth is directed belowground when water and nutrients are limiting and aboveground otherwise. Additional nutrients, such as N and P, increase shoot growth without equally increasing belowground biomass. Therefore foliar N concentration scales with root:shoot ratios and can be used to inform belowground biomass [35]. Conversely, the

isometric allocation growth model [42] suggests above- and belowground growth scale together as a result of physiological constraints. Consequently, nutrient addition stimulates total plant production, fertilizing above- and belowground biomass equivalently, leading to constant root:shoot ratios with respect to N concentration. As a result, according to this model, the relationship between foliar N and belowground growth would be less significant, but aboveground biomass would provide a better proxy.

Based on these growth models, remote-sensing of aboveground plant characteristics may provide the capability to scale up estimates of belowground biomass and root:shoot ratios. Optical remote-sensing using hyperspectral and multispectral imagery has been commonly used for mapping aboveground biomass [2,18,31,43,44]. Our earlier work explored the capacity of hyperspectral and multispectral sensors to estimate aboveground biomass within freshwater peat marshes of the Sacramento-San Joaquin Delta [21]. Canopy nutrient concentrations, such as foliar N, have also been modeled with remote-sensing data. These studies primarily used hyperspectral remote-sensing [1,45–47], but multispectral remote-sensing of foliar N also is growing more common [48–51]. Among multi-spectral sensors, Landsat 7 ETM+ may be especially useful for foliar N studies because it contains bands in the shortwave infrared wavelengths between 1550–1750 nm (band 5) and 2090–2350 nm (band 7) (landsat.usgs.gov). Wavelengths within these bands wavelengths have been associated with foliar N content within proteins, and represent N absorption features in the plant spectral signature [52]. In an earlier study we found that hyperspectral indices composed of these wavelengths correlated with foliar N in wetland plants [35]. We then explored remote-sensing-based indices of foliar N to model belowground biomass in these same marshes [35]. We compared whole plant productivity of *Schoenoplectus acutus (S. acutus*), a common freshwater macrophyte, across a simple experimental N-addition and control treatment. These data suggested *S. acutus* accumulates greater foliar N under environmental N enrichment. *S. acutus* also exhibited balanced growth because N-addition did not increase whole plant biomass, but shifted allocation from below to aboveground growth. Additionally, vegetation indices measured with a full spectrum field spectroradiometer differed among high and low N plants. Significant indices comprised bands at 550 nm (peak greenness), 1250 nm (corresponding to leaf water content), 1750 nm and 2100 nm (both corresponding to spectral N absorption features). These findings support the use of % foliar N as an indicator of belowground biomass and root:shoot ratios within *S. acutus* marshes. However extension to a field setting remains to be demonstrated.

Remote sensing of foliar N has challenges. Relationships among canopy N and spectral bands can be species-, season- and site-specific [53,54]. Species specific differences in plant canopy structure can cause confounding scattering in near infrared wavelengths, introducing noise into spectral relationships. For this reason, Knyazikhin *et al*. [53] particularly argued against mixed species modeling because these can cause spurious correlations in spectral N models. In this study we address these challenges through several means. First we selected study sites with low species diversity. In addition we explored single species *vs.* mixed species models, and we evaluated the physical basis for spectral foliar N models by building from our earlier experimental study and examining the contribution of key wavelengths.

2. Goals and Objectives

In this study, our goals were to identify variability in relative belowground biomass and biomass allocation ratios in a low diversity coastal freshwater marsh. We tested methods for scaling-up field estimates of belowground biomass and root:shoot ratios through remote-sensing of two aboveground plant characteristics, aboveground biomass and % foliar N, hypothesized to be related to belowground growth. As part of this test, we compared the effectiveness of multispectral satellite imagery from Landsat 7 to optimal remote-sensing data, hyperspectral field spectroradiometer data, for estimating % foliar N. Ultimately, our goals were to produce site-wide estimates of trends in belowground biomass and root:shoot ratios through a hybrid modeling approach that combined remote-sensing models of these two parameters. Additionally, for best fit

models, we evaluated error of mixed species *vs.* species specific modeling approaches for estimating relative differences in belowground biomass and root:shoot ratios.

3. Materials and Methods

3.1. Study Area

We sampled three impounded freshwater marsh ponds in the Sacramento-San Joaquin Delta, CA, USA: Twitchell Island east pond (38.1073°, −121.6483°), Twitchell Island west pond (38.1069°, −121.6449°), and Mayberry Slough southeast pond on Sherman Island (38.048953°, −121.766036°) (Figure 1). All ponds historically were part of extensive tidal freshwater perennial peat marshes of the Sacramento-San Joaquin River Delta (hereafter, "the Delta") and are hydrologically connected to San Francisco Bay. Like much of the Delta, our study sites were drained and cultivated with row crops beginning in the mid-1800s [6]. Draining resulted in oxidation and subsidence of deep peat soils to below sea level [55]. Our study areas have since been restored to freshwater wetland impoundments. The Mayberry pond was impounded in 1990, but was maintained as a seasonally drained moist-soil unit for waterfowl habitat over a 20-year period. Since 2010, the Mayberry pond was continuously inundated to establish permanent perennial vegetation. The Twitchell ponds were impounded in 1997 and managed to be permanently flooded. Twitchell ponds were 3 ha each and the Mayberry pond was 38 ha.

Elevation for these ponds ranges from 0.3–3 m below sea level (vertical datum: NAVD88), but levees and water control structures prevented uncontrolled flooding. Water depths were actively managed, but depth targets differed among ponds. Target depths were 55 cm above the soil surface for the Twitchell east and 25 cm for the Twitchell west pond. The Mayberry pond was larger, had more heterogeneous bottom morphology and had no target water depth. Water depths were managed by the California Department of Water Resources personnel through water control structures. Occasionally, some areas within ponds dried as a result of evapotranspiration before personnel arrived to alter water regimes. Water depth values actually measured in plots are provided in Table 1. The Twitchell west pond was shallow and exhibited the narrowest range in water depths.

Table 1. Mean vegetation and physical parameters measured within our wetland impoundments (95% confidence interval in parentheses). Percent *Schoenoplectus acutus* (*S. acutus)* and percent *Typha* spp. are the percentage of live emergent vegetation that was comprised of each species. Cover of *S. acutus*, *Typha*, thatch and a combined water/floating aquatic vegetation class are the percent aerial cover of plots for each cover type. Water depths were measured within plots relative to the soil surface.

Parameter	Twitchell West	Twitchell East	Mayberry
Percent *S. acutus*	38 (0–100)	52 (0–100)	1 (0–7)
Percent *Typha* spp.	62 (0–100)	48 (0–53)	99 (92–100)
S. acutus cover	12 (0–38)	18 (0–53)	1 (0–6)
Typha cover	23 (0–62)	22 (0–69)	58 (10–100)
Thatch cover	61 (24–98)	54 (13–94)	22 (0–65)
Thatch height (cm)	106 (22–189)	93 (0–202)	81 (0–167)
Water/Aqu. veg cover	4 (0–22)	7 (0–31)	20 (0–57)
Water depth (cm)	7 (0–30)	6 (0–38)	25 (0–66)

Emergent vegetation in all three ponds was mostly *S. acutus* and *Typha domingensis* (*T. domingensis*), *T. latifolia, T. angustifolia* and *Typha* spp. hybrids. Vegetation was not planted at the time of restoration within Mayberry, but passively colonized the site. At the time of sampling at Mayberry, 2 years post restoration, cover was largely dominated by *Typha* spp. with smaller amounts of *S. acutus* intermingled. Within the Twitchell ponds, *S. acutus* was planted at the time of restoration and was more abundant during our sampling (15 years post restoration). Areas of open

water and submerged aquatic vegetation (predominantly *Lemna sp.*) also were present in all ponds. *S. acutus* and *Typha* spp. are emergent wetland perennial herbaceous vegetation. These species go dormant over the winter, senescing aboveground vegetation and initiating new shoots in spring.

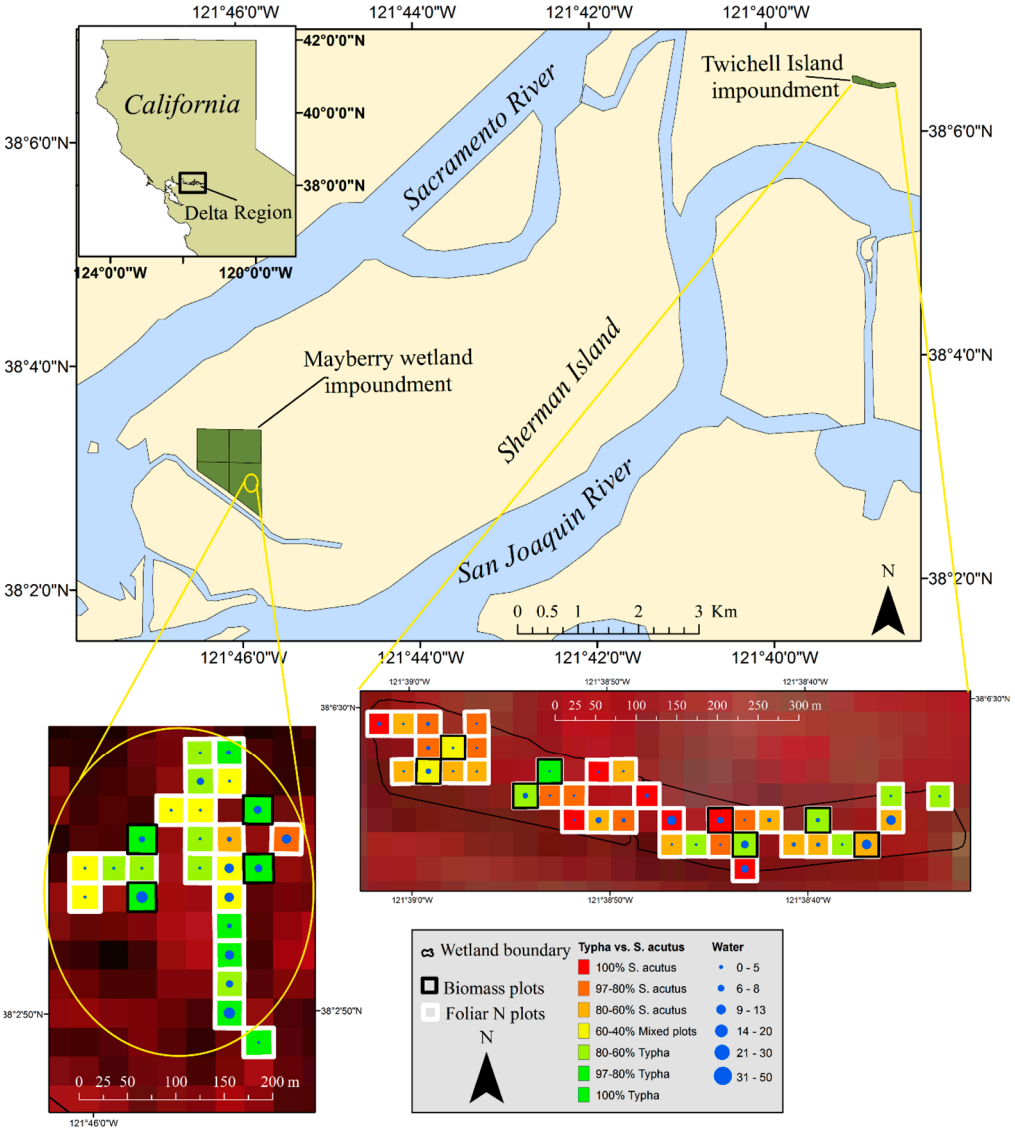

Figure 1. The Sacramento-San Joaquin Delta, CA, USA, showing locations of studied wetland impoundments. Insets show biomass and foliar N plots within study sites, superimposed over a Landsat 7 false color (Near infrared, Red and Green bands shown as RGB channels). Symbols indicate average water depth (cm) and relative percent cover of *Typha* spp. *vs. S. acutus* as measured overtime during our study.

3.2. Data Collection

We estimated above- and belowground emergent wetland plant biomass and % foliar N using field methods during one summer growing season. We measured these parameters within 30 m × 30 m permanent plots that corresponded with Landsat 7 pixel footprints. We used these data to build statistical relationships between vegetation parameters and spectral reflectance. We sampled four 30 m × 30 m biomass plots per wetland impoundment for a total of 12 biomass plots (Figure 1).

3.2.1. Measurement of Belowground Biomass

To estimate above- and belowground biomass within the 30 m × 30 m plots, we established 3 permanent 1 m² vegetation sub-plots 12.5 m apart along transects that spanned plot widths. To

measure belowground biomass, we installed 1 to 3 ingrowth root cores [56,57] in each sub-plot on 20 April 2012. Overall there were 24 ingrowth root cores per wetland pond and 72 root cores total. We used a 10.2-cm diameter corer [58] to excavate a 30-cm deep cylindrical hole from the marsh peat substrate. We secured in each cavity an ingrowth root core, consisting of a 30 cm × 10 cm mesh bag (mesh size 3 mm) filled with peat moss (Sungro Horticulture, Vancouver, BC, Canada). We filled ingrowth cores with peat moss to minimize differences in media within cores compared to the surrounding peat marsh substrate. Hereafter we use belowground biomass to refer to biomass estimated from root cores and these estimates should be considered to reflect relative differences in root and rhizome biomass among sample locations, rather than total production.

We used a Trimble GeoXT hand-held sub-meter GPS with field computer (Trimble Navigation Limited, Sunnyvale, CA, USA) to record root core locations with sub-meter accuracy. Cores were collected following peak biomass development on 26 September 2012 (6 months of growth). Following core collection, plant material within cores was sorted into roots and rhizomes, live *vs.* dead material, and by genus (*Typha vs. Schoenoplectus*). Roots can be distinguished by genus through color and morphology differences: *S. acutus* roots were milky white or reddish. *S. acutus* rhizomes also were reddish and had a textured, segmented appearance. *Typha* spp. roots and rhizomes were creamy yellow in color and smooth. We oven-dried plant material at 40 °C until all tissue moisture was removed. We focused subsequent analysis on these oven-dried weights. We scaled oven-dried belowground biomass from root cores to $g \cdot m^{-2}$ to 30 cm depth. All samples within a plot (our sample unit) were then averaged to a single end of season belowground biomass $g \cdot m^{-2}$ estimate. End of season root:shoot ratios were calculated using biomass estimates from ingrowth root cores and aboveground allometric measurements averaged within each 1 m^2 sub-plot.

3.2.2. Measurement of Aboveground Biomass

We measured aboveground biomass and cover three times (July, August, and September 2012) within each permanent 1 m^2 sub-plot using non-destructive methods in order to generate a multi-temporal remote-sensing model of aboveground plant biomass. Within 1 m^2 sub-plots, we estimated percent cover of water, bare ground, dead vegetation, submerged aquatic vegetation and cover of *S. acutus* and *Typha* spp. We also counted all plant stems, measured water depth and height of accumulated dead thatch. For aboveground biomass estimation, we used allometric equations established by Miller and Fujii [59] to derive weights of all plants from within a 0.1 m^2 quadrat centered directly over ingrowth root cores within the 1 m^2 sub-plots. Explained variance (R^2) for the *S. acutus* allometric model in Miller and Fujii's [59] study was 0.92; R^2 for the *T. latifolia* model was 0.9, and R^2 for the T. *angustifolia*/*T. domingensis* model was 0.92. Neither the time of sample collection nor water depth affected the allometric relationships in Miller and Fujii's study.

Aboveground biomass of plants within 0.1 m^2 quadrat were summed and then scaled to $g \cdot m^{-2}$. To account for differences in plant density among quadrats and larger sub-plots, we applied a correction factor consisting of the ratio of stem density in the quadrat *vs.* the 1 m^2 sub-plot. To derive final estimates, sample sub-plots within the same 30 m plot were averaged together to generate a single $g \cdot m^{-2}$ estimate for each plot and sample date, generating 36 samples overall.

3.2.3. Measurement of Foliar Nitrogen Concentration

We also measured foliar N to build empirical models of % foliar N first from hyperspectral field spectroradiometer reflectance data and then from satellite imagery. We collected 158 leaf samples for foliar N across each wetland from 2 sampling periods (mid-summer and end of growing season). Foliar N sample locations were within our permanent 30 m × 30 m plots plus additional 30 m × 30 m plots to increase foliar N sample size and increase coverage across ponds. Additional foliar N plots were possible because sampling for this dataset is less labor intensive than biomass sampling. Foliar N plots were spread evenly throughout each pond (Figures 1 and 2). Foliar N sample locations also were located along wetland boardwalks, platforms and berms to allow access with the field spectroradiometer for hyperspectral measurements and to avoid disturbing biomass sampling locations. We used the Trimble GeoXT hand-held sub-meter GPS to record foliar N plots.

Oven-dried plant leaves were measured for elemental concentration of total N at the USGS Menlo Park Stable Isotope lab (Menlo Park, CA, USA). The USGS Menlo Park laboratory uses a Micromass Optima mass spectroradiometer connected to a Carlo Erba NA 1500 elemental analyzer. Hereafter we use % foliar N to mean % by weight of foliar tissue that was N (organic + inorganic N). For satellite models, as above, all foliar N estimates within the same Landsat pixel were averaged together to generate a single estimate (1–5 leaf samples per plot).

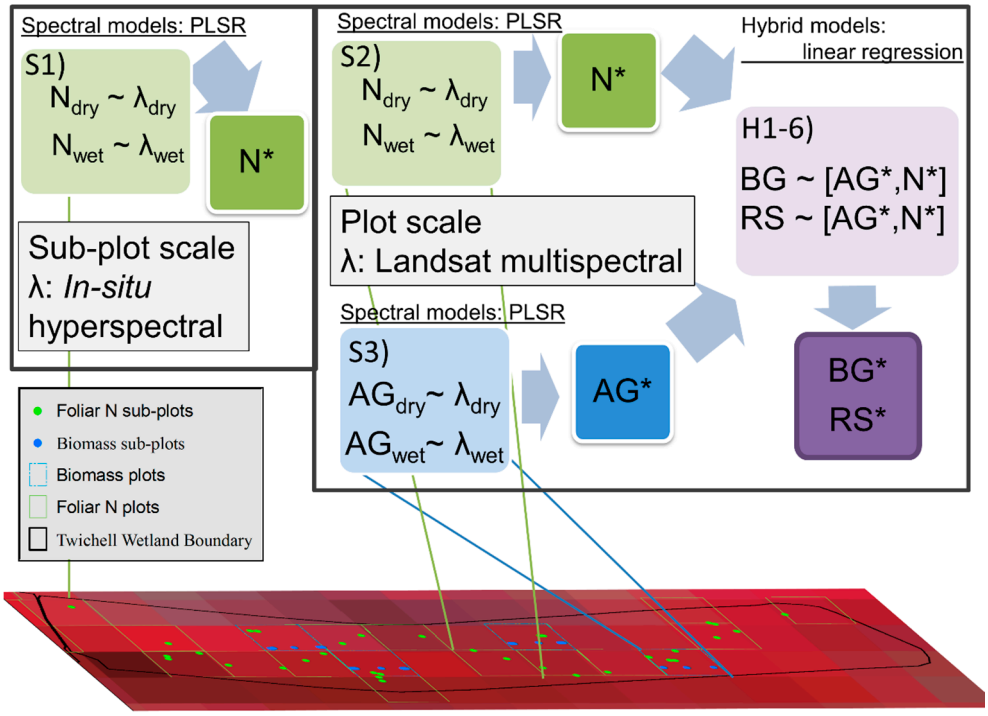

Figure 2. Model building process for estimating belowground biomass (BG) and root:shoot ratio (RS) from spectral reflectance (λ) estimates of aboveground biomass (AG) and foliar nitrogen (N). Foliar N and aboveground biomass models were built separately for flooded and non-flooded plots and the best estimates for each plot were joined back into a single dataset. Prediction of belowground biomass or root:shoot ratio was conducted at the plot scale only. * indicates spectrally derived estimates and quantities without asterisks are field derived estimates. Model numbers refer to those listed in Table 2.

Table 2. Remote-sensing-based models of % foliar N and aboveground biomass (Spectral model sets S1–S3) and hybrid models of belowground biomass and root:shoot ratio (Hybrid model sets H1–H6), which use reflectance estimated predictors from spectral model sets.

Model Set	Model Description
	PLS regression spectral reflectance models
S1	Predicted % foliar N ~ Hyperspectral reflectance
S2	Predicted % foliar N ~ Multispectral Landsat 7 reflectance
S3	Predicted aboveground biomass ~ Multispectral Landsat 7 reflectance
	Hybrid models
H1	Field belowground biomass ~ Predicted N (model S2)
H2	Field belowground biomass ~ Predicted aboveground biomass (model S3)
H3	Field belowground biomass ~ Predicted aboveground biomass (model S3) + Predicted N (model S2)
H4	Field root:shoot ratio ~ Predicted N (model S2)
H5	Field root:shoot ratio ~ Predicted aboveground biomass (model S3)
H6	Field root:shoot ratio ~ Predicted belowground biomass (best from models H1-H3)/Predicted aboveground biomass (model S3)

3.2.4. Field Spectroradiometer Reflectance Data Collection

To build hyperspectral models of % foliar N, we collected *in situ* hyperspectral reflectance using an ASD field spectroradiometer (FieldSpec Pro FR, Analytical Spectral Devices, Inc., Boulder, CO, USA) (Figure 2). ASD spectral readings were narrowband full spectrum measurements, sampled every 1.4 nm over 350–1000 nm and 2 nm over 1000–2500 nm. We used a 25° field of view foreoptics at nadir 1 m above the vegetation canopy and 4 m from ground level, using a 3 m fiber optic cable producing a field of view of 1.8 m. We calculated canopy reflectance as the ratio of canopy radiance to radiance measured from a calibrated white reference (Spectralon® Labsphere, Inc., North Sutton, NH, USA). We collected white reference measurements every 10 min. Ten reflectance measurements, each an average of 12 spectra, were collected and averaged using ViewSpec™ Pro 6.1.10 (Analytical Spectral Devices, Inc., Boulder, CO, USA). We preprocessed spectroradiometer reflectance by removing wavelengths with high noise from water absorption features and averaged reflectance to spectral bands 10 nm wide, resulting in 164 hyperspectral bands. The resulting bands covered the ranges 422–1300 nm, 1443–1795 nm, and 1998–2400 nm. These field-collected hyperspectral bands represent high resolution full-spectrum data without atmospheric scattering. They provide a point of comparison for precision lost when using other remote-sensing platforms, such as Landsat 7.

3.2.5. Landsat Image Acquisition and Processing

We used Landsat 7 Climate Data Record surface reflectance images that corresponded to field sample dates (24 June, 10 July, 26 July, 11 August, 27 August, 28 September, and 10 October, 2012) (available via earthexplorer.usgs.gov). These images are atmospherically corrected surface reflectance data products processed by USGS using the Landsat Ecosystem Disturbance Adaptive Processing System (LEDAPS) algorithm [60]. We did not gap fill areas of no data within Landsat 7 imagery, but left these as missing values. Landsat images were georeferenced with ground control points and converted to UTM projection (NAD83, Zone 10N) using bilinear resampling within ArcGIS 10.1 (ESRI Corporation, Redlands, CA, USA). We collected ground control points with a sub-meter accurate Trimble GeoXT. Root mean square error of georeferencing for rectified images was less than half pixel size for each image.

3.3. Development of Models for Estimating Relative Differences in Belowground Biomass

To derive relationships among belowground biomass, foliar N and aboveground biomass, we first used *in situ* hyperspectral data to build empirical models of % foliar N. We used *in situ* and satellite-based spectral estimates of foliar N and aboveground biomass to derive site-wide models of belowground biomass and root:shoot ratio.

3.3.1. Remote-Sensing-Based Estimates of Aboveground Biomass and % Foliar N

We used our multi-temporal field collected measures of % foliar N and aboveground biomass to generate remote-sensing-based estimates of these same variables (*Spectral* model sets S1–S3, Table 2, Figure 2). Models were developed for % foliar N with field spectrometer and Landsat 7 reflectance data, and for aboveground biomass with Landsat 7 reflectance data. We sub-divided data for each model into flooded and unflooded plots and analyzed these separately. Flooding can dampen spectral reflectance, particularly near infrared reflectance [27,28]. We therefore compared models where flooded and unflooded samples were separated to analyses of the full dataset. Then, we recombined the predicted outcomes from these models into a new dataset that contained the best spectral prediction for each parameter for each sample. These spectral estimates could then be used as predictors in our belowground biomass hybrid modeling efforts below.

To build the spectral datasets of foliar N and aboveground biomass in Figure 2 and Table 2, we used the PLS package in R [61] to derive partial least squares (PLS) regression models estimating % foliar N and aboveground biomass (each separately). To select PLS components, we choose those that corresponded to the first local minima for root mean squared error of prediction (RMSEP,

e.g., averaged difference in predicted *vs.* measured values) because this minimizes model over-fitting [61]. RMSEP was estimated using leave-one-out cross validation [61]. We also calculated normalized RMSEP (nRMSEP = RMSEP/[response maximum–response minimum]), which approaches zero for better models and 1 for poor models. nRMSEP allows performance comparison across different datasets. To develop models, we used a random subset as training data (70% of samples) and calculated R^2 or explained variance, RMSEP and nRMSEP. We compared R^2, RMSEP and nRMSEP from the training set to those same metrics calculated over a testing dataset (30% of samples). For all models, loadings plots for the first 3 PLS regression components (*i.e.*, those explaining the majority of variance) were examined to determine wavelengths most associated with response variables (% foliar N and aboveground biomass).

We also compared species specific and mixed species models. We defined species specific models as models of plots where the target species was at least 20% of the live vegetation cover. We selected 20% as our cut-off because this excludes plots where the model species had very low to no cover, but still allows heterogeneity that can introduce noise into reflectance signals.

3.3.2. Hybrid Model Development: Estimating End of Season Belowground Biomass Trends from Remote-Sensing Estimates of Aboveground Biomass and Foliar N

To develop site-wide models of end of season belowground biomass and root:shoot ratio (*Hybrid* model sets H1–H6, Table 2, Figure 2), we used the spectral reflectance model sets of % foliar N and aboveground biomass (S2–S3, Table 2). While all sample dates were used to build the best spectral models for % foliar N and aboveground biomass, only end-of season spectral estimates were used to predict end of season belowground biomass. We used the best end of season predictions for each plot from our foliar N and aboveground biomass reflectance models as predictors in linear regressions where belowground biomass or root:shoot ratios were response variables. These hybrid reflectance models for predicting relative differences in belowground biomass and root:shoot ratio included all possible combinations of foliar N and aboveground biomass including single parameter models and dual parameter models, including interaction terms. We explored species specific and mixed species models in each model set as above. We also explored possible non-linear relationships among parameters through log transformations of predictors and response variables.

To calculate parameter confidence, we used a bootstrapping approach with bias-corrected and accelerated confidence intervals [62] to compare model performance across 9999 permutation of the data. To document model error, we used leave-one-out cross-validation to estimate RMSEP and nRMSEP model estimates *vs.* field measured values.

We removed plots where the measured target response variable was minimal. For biomass models, plots with less than 10 $g \cdot m^{-2}$ were excluded. For root:shoot ratio models, ratios of less 0.01, *i.e.*, samples with very little target root material, also were excluded.

We selected the best hybrid model for estimating belowground biomass and root:shoot ratio for all species and for each species individually. Criteria for identifying the best model were (1) the model could not contain multi-collinear predictors; (2) the 95% confidence interval for model slopes could not overlap zero; and (3) of the remaining models, the best one had the highest explained variance and lowest nRMSEP.

4. Results

Foliar N concentration ranged from 0.5 to 4.4 g N per 100 g dry leaf tissue (mean: 2.6; SD: 0.7; 158 samples). Standard deviation of foliar N samples from within the same sample plot was 0.21. End of season belowground biomass was greater for *S. acutus* than for *Typha* spp. (Table 3). Conversely, end of season aboveground biomass was greater for *Typha* spp. (Table 3).

Table 3. Mean and range of field measured and Landsat reflectance based estimates of end of season biomass ($g \cdot m^{-2}$) and root:shoot ratio across all wetland impoundments. Values were calculated from nonzero samples.

Parameter	Scale	Mean	SD	Min	Max
	S. acutus				
Belowground biomass	Field: 1 m² sub-plot	519	571	2.5	2316
	Field: 30 m × 30 m	270	274	12.7	762
	Landsat: 30 m × 30 m	395	278	11	691
Aboveground biomass	Field: 1 m² sub-plot	346	179	72	653
	Field: 30 m × 30 m	216	123	44	431
	Landsat: 30 m × 30 m	308	81	189	442
Root:shoot ratio	Field: 1 m² sub-plot	2.5	2.2	0.1	7.8
	Field: 30 m × 30 m	2.1	2.9	0.1	7.7
	Landsat: 30 m × 30 m	2.6	2.5	0.9	6.0
	Typha spp.				
Belowground biomass	Field: 1 m² sub-plot	98	172	1	918
	Field: 30 m × 30 m	102	88	22	329
	Landsat: 30 m × 30 m	102	55	25	166
Aboveground biomass	Field: 1 m² sub-plot	653	589	20	2259
	Field: 30 m × 30 m	625	476	119	1512
	Landsat: 30 m × 30 m	550	386	119	1061
Root:shoot ratio	Field: 1 m² sub-plot	0.3	0.2	0.1	1.2
	Field: 30 m × 30 m	0.3	0.4	0.1	1.1
	Landsat: 30 m × 30 m	0.3	0.2	0.1	0.7

4.1. Foliar N and Aboveground Biomass Spectral Reflectance PLS Regression Models

4.1.1. Hyperspectral Reflectance Models

Spectral signatures of *Typha* spp. and *S. acutus* were plotted and had subtle differences in visible (500–600 nm), near infrared (800–1000 nm) and shortwave infrared (>1500 nm) wavelengths (Figure 3). Reflectance correlated well with % foliar N, based on PLS regression of all spectral bands for both species specific and mixed species models (Table 4). Analyzing flooded and unflooded plots separately improved explained variance from 45%–56% for the full data set for species specific models (data not shown) to 54%–90% (Table 4). Models for *Typha* spp. explained greater variance in % foliar N than other models.

Figure 4 shows loadings plots from these hyperspectral foliar N analyses. Bands that are given a high weight in the calculation of components have a high absolute value (either positive or negative) in the loadings plots. Bands associated with green and red spectra between 525–750 nm, near infrared spectra between 1100–1300 nm, and shortwave infrared spectra >1600 nm were important for associating % foliar N with hyperspectral reflectance. Bands with high absolute values in loadings varied by PLS component. Component 1, which contains the majority of explained variance between predictors and response, closely mirrors the spectral signature of the target species within both species (Figures 3 and 4). For *Typha*, Component 2, possibly the component most associated with % foliar N, had high absolute loadings values for spectra associated with the red-edge (740–770 nm), with near infrared spectra between 900–1100 nm, and with shortwave infrared spectra, especially at 1600 and 2100 nm. Similarly, within *S. acutus* loadings plots (Figure 4), Component 1 mirrored the spectral signature of *S. acutus*, but contained less of the explained variance than did *Typha* component 1. Component 2 had high absolute loadings at the red edge (750 nm), at 900 and 1100 nm and then in the shortwave infrared spectra >1600 nm.

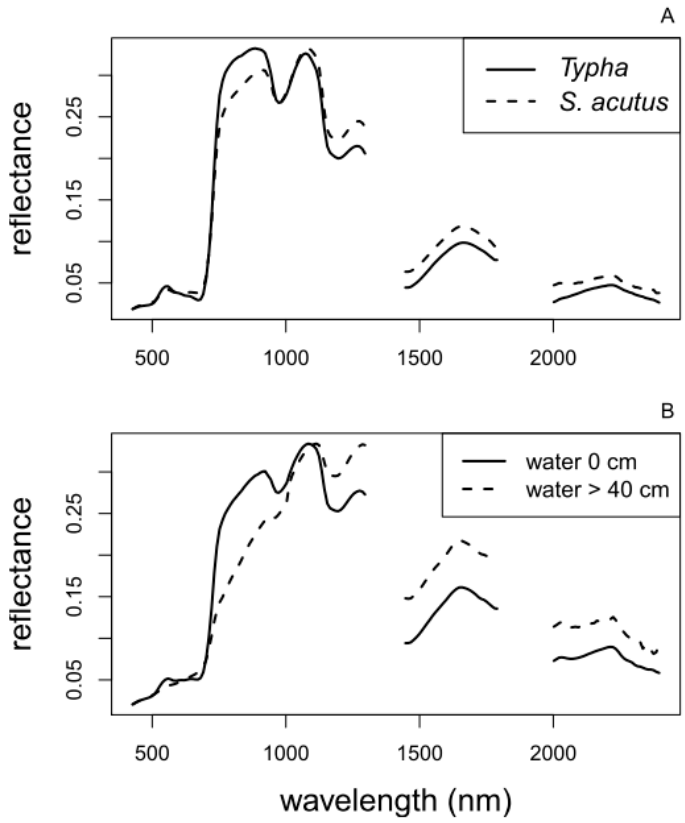

Figure 3. Spectral signature of *Typha* spp. and *S. acutus* (all water depths) (**A**) and of flooded and unflooded plots (both species combined) (**B**) from freshwater marsh impoundments in the Sacramento-San Joaquin Delta, CA, USA. Gaps indicate areas of noise in the spectra that were removed during pre-processing.

4.1.2. Multispectral Reflectance Models

Multispectral Landsat 7 satellite reflectance had relationships with % foliar N for all models. Analyzing flooded and unflooded plots separately increased explained variance. For example, species specific models of all data combined explained 27%–47% of variance (results not shown), whereas models of unflooded plots explained 50%–70% of variance (Table 4). For multispectral analyses, unflooded plots had greater explained variance than flooded plots. For *Typha* spp., Landsat compared to *in situ* hyperspectral data reduced explained variance (hyperspectral 54%–90% explained variance across flooded and unflooded plots, multispectral 50% unflooded, 24% flooded, Table 4, Figure 5). Conversely, species specific models of *S. acutus* retained explanatory power equivalent to hyperspectral models (explained variance hyperspectral 62%–63% across flooded and unflooded plots, multispectral 70% unflooded, 42% flooded, Table 4, Figure 5).

PLS regression models of Landsat 7 reflectance also estimated aboveground biomass with moderate precision for both mixed species and species specific models, (explained variance 53%–67%, Table 4). *S. acutus* models outperformed *Typha* and mixed species models (Table 4). Subsetting by water depth did not improve aboveground biomass model accuracy, likely because sample size was too low after subsetting, allowing little room for creating testing and training datasets (sample size was eight and five, respectively, for *Typha* and *S. acutus* aboveground biomass models, see Table 4 model set S3).

Table 4. Mixed species and species specific PLS regression models of % foliar N and aboveground biomass (AG) (g) from field spectroradiometer-based hyperspectral and satellite-based multispectral reflectance. Model set numbers refer to Table 2. C is the number of PLS regression components, EV (% explained variance), RMSEP (root mean square error of prediction), nRMSEP (normalized RMSEP) and *N* is sample size for each analysis. Hyperspectral models of aboveground biomass can be found in Byrd *et al.* [21]. Hyperspectral models used 1 m² sub-plot level data, while Landsat models used plot-scale data (30 m × 30 m).

Model			Water depth	Training C.	EV	RMSEP	nRMSEP	*N*	Testing RMSEP	nRMSEP	*N*
S1a.	% N mixed	= hyperspectral reflectance	0	4	54	0.46	0.20	37	0.52	0.23	12
			>0	14	83	0.56	0.15	76	0.90	0.28	28
S1b.	% N *Typha* sp.	= hyperspectral reflectance	0	7	90	0.50	0.24	19	0.57	0.28	4
			>0	6	54	0.53	0.17	48	0.83	0.24	18
S1c.	% N *S. acutus*	= hyperspectral reflectance	0	3	63	0.45	0.26	15	0.43	0.33	4
			>0	4	62	0.47	0.23	23	0.48	0.31	7
S2a.	% N mixed	= Landsat reflectance	0	5	56	0.49	0.25	32	0.51	0.25	12
			>0	3	27	0.68	0.19	67	0.59	0.18	25
S2b.	% N *Typha* sp.	= Landsat reflectance	0	3	50	0.56	0.24	19	0.18	0.14	4
			>0	3	24	0.68	0.18	50	0.83	0.21	20
S2c.	% N *S. acutus*	= Landsat reflectance	0	3	70	0.43	0.26	14	0.43	0.26	4
			>0	3	42	0.55	0.29	20	0.44	0.24	4
S3a.	AG mixed	= Landsat reflectance	all	4	53	433.3	0.14	25	773.4	0.25	10
S3a.	AG *Typha* spp.	= Landsat reflectance	all	3	59	448.2	0.24	21	309.3	0.25	8
S3c.	AG *S. acutus*	= Landsat reflectance	all	2	67	155.5	0.20	12	262.7	0.34	5

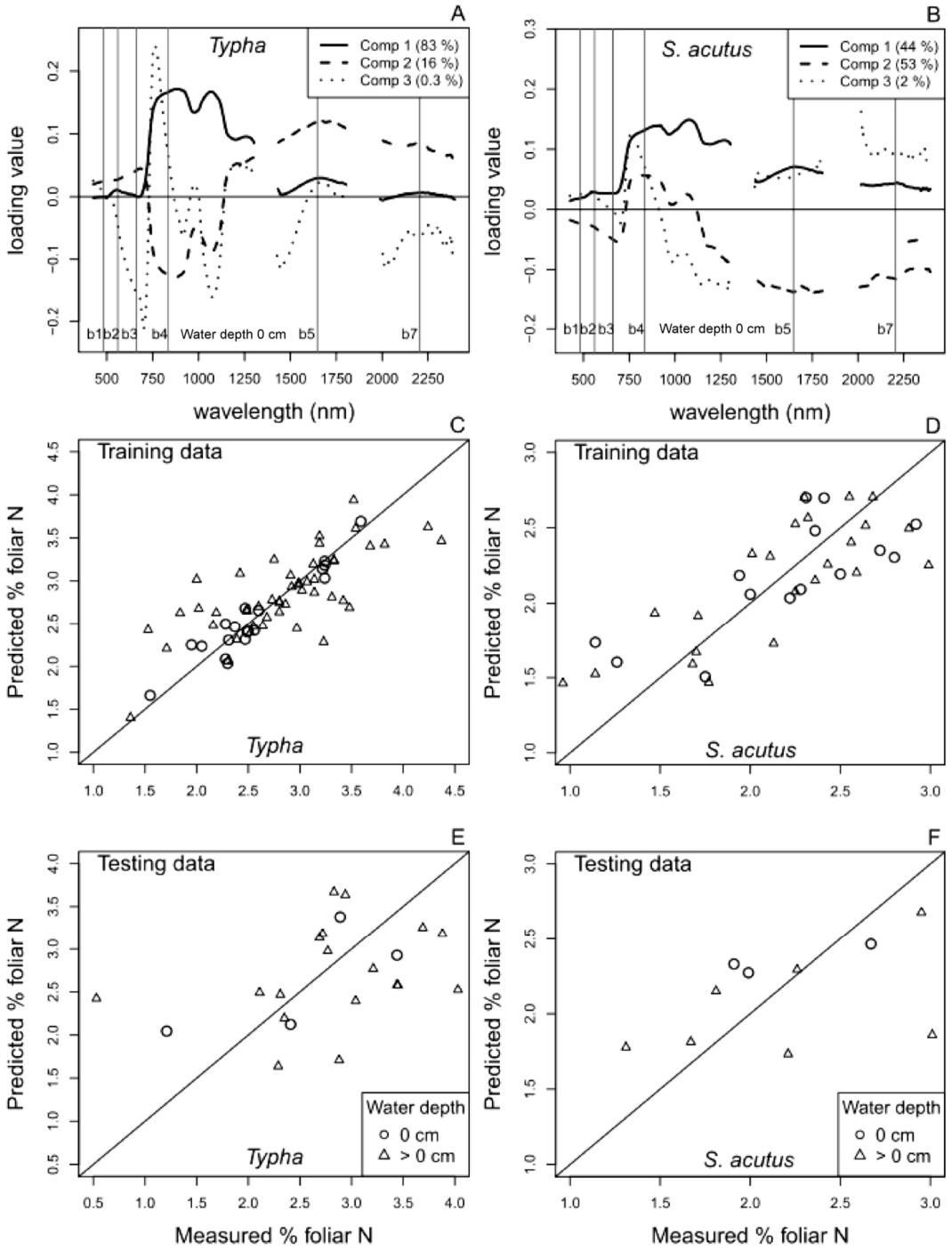

Figure 4. Loadings values of % foliar N from PLS regression of hyperspectral data for (**A**) *Typha* spp. and (**B**) *S. acutus* (model set S1). Gaps indicate spectra removed during pre-processing. The mid-point of Landsat 7 bands are superimposed and labeled with band number (b1-7). (**C**–**F**) Measured *vs.* predicted values for training and testing data for *Typha* and *S. acutus*.

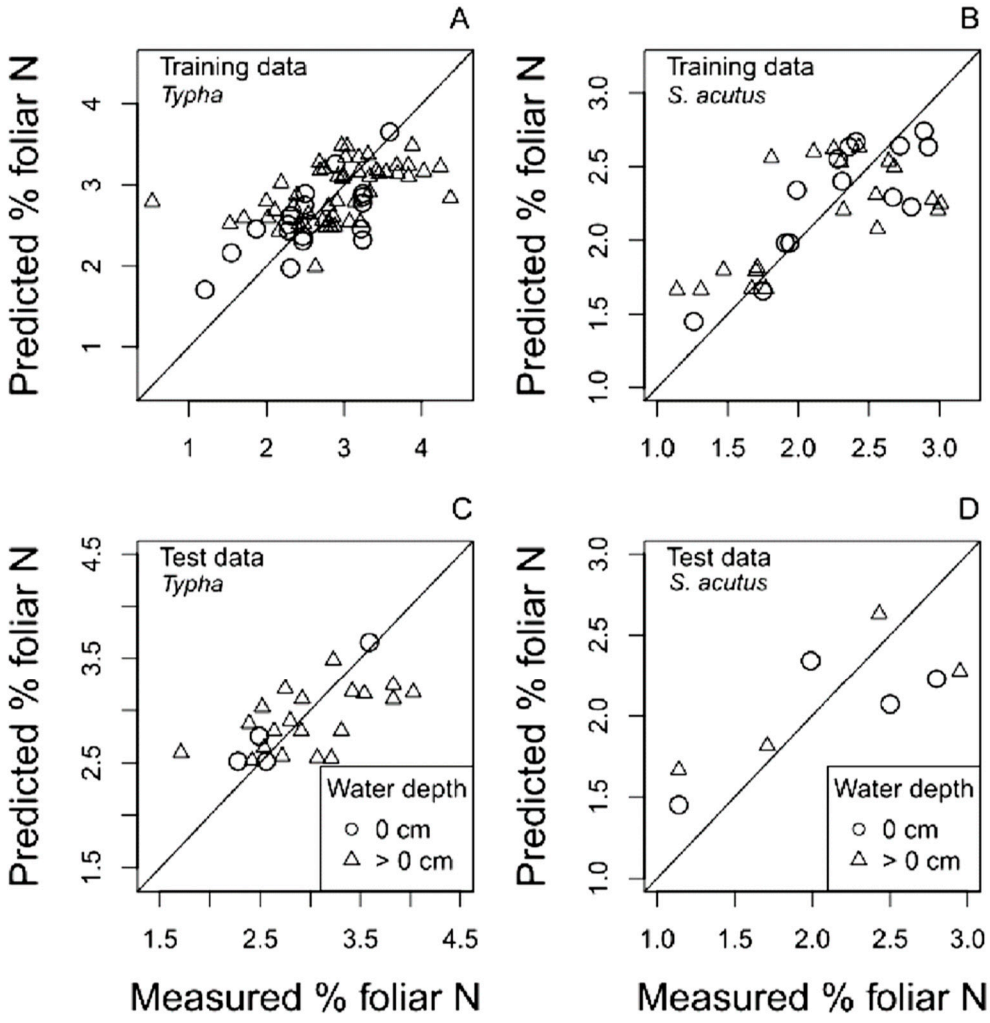

Figure 5. Measured *vs.* % foliar N developed from PLS regression of Landsat 7 for training (**A**,**B**) and testing (**C**,**D**) data for *Typha* spp. and for *S. acutus* (model set S2). Percent foliar N is in g N per 100 g dry leaf tissue.

Landsat 7 bands corresponded with some PLS regression loadings peaks and valleys for % foliar N, particularly in the shortwave infrared spectra, bands 5 (1550–1750 nm) and 7 (2080–2350 nm) (Figure 4). However, other spectra in the hyperspectral dataset with high absolute loadings were missed, particularly those at 1000–1250 nm (Figure 4).

4.2. Predicting Trends in Belowground Biomass and Root:Shoot Ratio Using Satellite-Derived Multispectral Reflectance Hybrid Models

4.2.1. Belowground Biomass Hybrid Models

Many hybrid models relating spectral reflectance estimates of aboveground plant characters to belowground biomass were statistically significant (Table 5; Figure 6). The best models were species specific. For *S. acutus*, belowground biomass had negative relationships with both % foliar N and aboveground biomass, but the best predictor was aboveground biomass (explained variance 76%, RMSEP 140 g, nRMSEP 0.19) (Figure 6). In contrast, for *Typha* spp., only % foliar N was a good predictor and explained variance was lower (39%, RMSEP 65 g, nRMSEP 0.21) (Figure 6). For all model sets, models combining aboveground biomass and % foliar N as predictors did not meet our selection criteria, either because p-values were not significant or the 95% confidence interval for parameters overlapped zero. Interaction terms among % foliar N and aboveground biomass also were not significant.

Table 5. Hybrid models of end of season belowground biomass and root:shoot ratio, where model set numbers refer to Table 2. Predictors for model sets were spectral estimates (source model number from Table 4 in parentheses). The best models are in bold (see methods for criteria). Legend: Belowground biomass (BG) (g), root:shoot ratio (RS), aboveground biomass (AG) (g), *N* is the sample size, F is the *F* statistic, df is degrees of freedom, *P* is the p-value, EV (% explained variance), β_0 is the intercept, β_{1-2} are parameter slopes, where β_1 is for the first parameter under predictors and β_2 is for the second (if present). L_{0-2} and H_{0-2} are the lower and upper bounds for the 95% confidence interval for each coefficient as calculated by bootstrapping across 9999 permutations of the data.

Model	Predictors	*N*	*F*	df	*P*	RMSEP	nRMSEP	EV	β_0	L_0	H_0	β_1	L_1	H_1	β_2	L_2	H_2
Mixed spp. models																	
H1a. BG ~	**log(%N) (S2a)**	**12**	**3.4**	**1,10**	**0.094**	**231.1**	**0.29**	**26**	**571**	**282**	**943**	**−430**	**−904**	**−12**	**-**	**-**	**-**
H2a. BG ~	AG (S3a)	12	2.3	1,10	0.163	241.6	0.3	19	1550	−16	3254	−199	−446	73	-	-	-
H3a. BG ~	AG (S3a) + log(%N) (S2a)	12	1.6	2,9	0.248	229.3	0.29	27	950	−807	3414	−69	−465	283	−342	−1088	327
H4a. RS ~	**log(%N) (S2a)**	**12**	**6.9**	**1,10**	**0.026**	**0.4**	**0.27**	**41**	**1.7**	**0.8**	**2.6**	**−0.6**	**−1.0**	**−0.2**	**-**	**-**	**-**
H5a. RS ~	AG (S3a)	12	3.1	1,10	0.111	0.5	0.31	23	1.0	0.5	1.7	−0.0	−0.0	0.0	-	-	-
H6a. RS ~	BG (H1a)/AG (S3a)	12	2.8	1,10	0.126	0.5	0.31	22	0.3	0	0.8	0.3	0.1	0.8	-	-	-
Typha spp. models																	
H1b. BG ~	**log(%N) (S2b)**	**10**	**5.1**	**1,8**	**0.053**	**64.6**	**0.21**	**39**	**294**	**148**	**516**	**−242**	**−442**	**−14**	**-**	**-**	**-**
H2b. BG ~	AG (S3b)	9	2.7	1,7	0.145	71.4	0.23	28	171	109	308	−0.1	−0.2	0.1	-	-	-
H3b. BG ~	AG (S3b) + log(%N) (S2b)	9	5.2	2,6	0.048	50.9	0.17	64	592	172	958	0.4	−0.1	0.9	−848	−1698	−142
H4b. RS ~	**log(%N) (S2b)**	**10**	**47.7**	**1,8**	**<0.001**	**0.3**	**0.24**	**86**	**2.5**	**1.4**	**4.1**	**−5.4**	**−7.0**	**−4.0**	-	-	-
H5b. RS ~	AG (S3b)	10	5.0	1,8	0.056	0.3	0.26	38	0.6	0.4	1.1	−0.0	−0.0	0.0	-	-	-
H6b. RS ~	BG (H1b)/AG (S3b)	9	4.5	1,7	0.071	0.3	0.26	39	0.1	−0.1	0.6	0.6	0	1.2	-	-	-
S. acutus models																	
H1c. BG ~	log(%N) (S2c)	8	5.9	1,6	0.052	212.6	0.29	49	8	6	11	−4	−9	−1	-	-	-
H2c. BG ~	**AG (S3c)**	**5**	**9.5**	**1,3**	**0.054**	**136.7**	**0.18**	**76**	**1196**	**512**	**1648**	**−2**	**−5**	**−1**	**-**	**-**	**-**
H3c. BG ~	AG (S3c) + log(%N) (S2c)	5	4.5	2,2	0.181	119.3	0.16	82	388	−2044	2237	−3	−5	−1	1515	−2264	5282
H4c. RS ~	log(%N) (S2c)	5	0.5	1,3	0.537	2.5	0.33	14	−9.0	−38.1	23.7	22.4	−40.0	79.6	-	-	-
H5c. RS ~	AG (S3c)	5	6.0	1,3	0.093	1.6	0.21	67	9.8	4.0	16.9	−0.0	−0.1	−0.0	-	-	-
H6c. RS ~	**BG (H2c)/AG (S3c)**	**5**	**11.9**	**1,3**	**0.041**	**1.2**	**0.16**	**80**	**−0.5**	**−2.9**	**1.8**	**1.8**	**0.7**	**2.8**	**-**	**-**	**-**

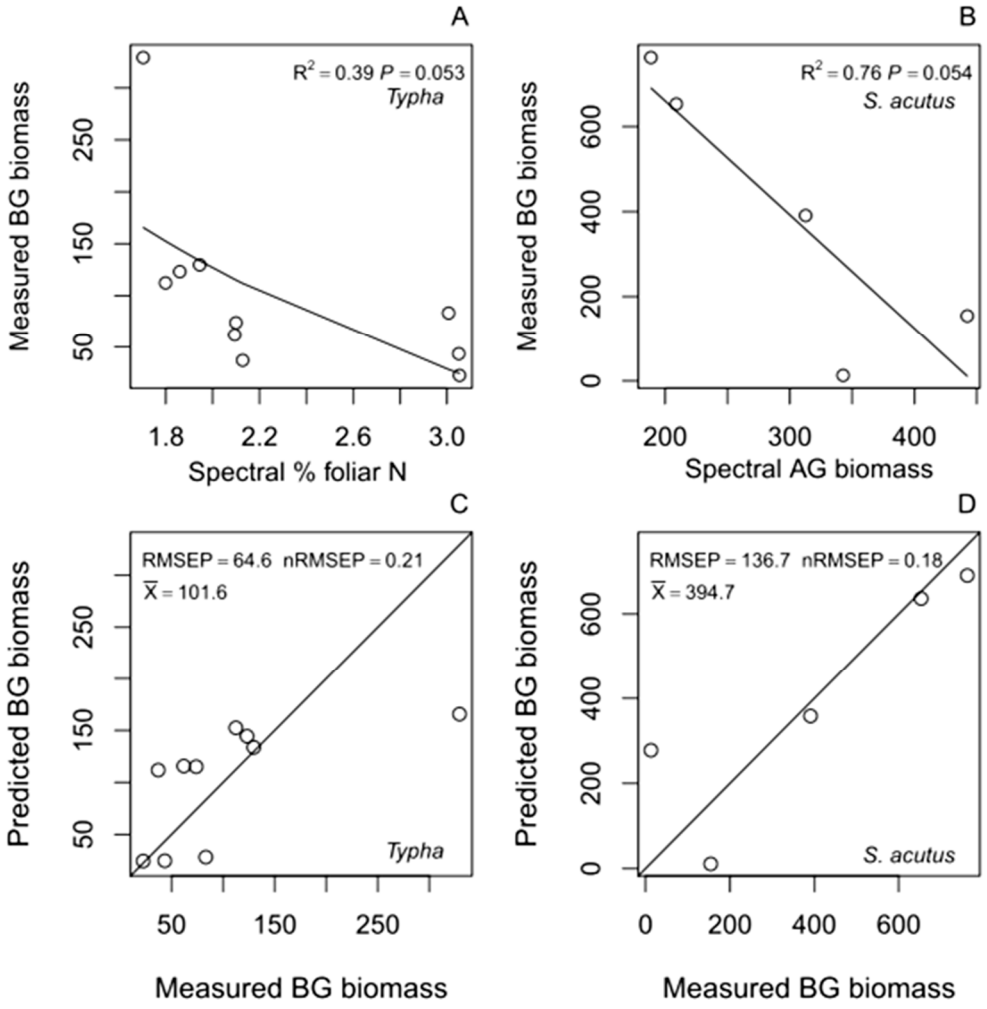

Figure 6. (**Left**) *Typha* spp. best belowground biomass (g·m^{-2}) model (model H4b, % foliar N (**A**) is the predictor). (**Right**) *S. acutus* best belowground biomass (g·m^{-2}) model (model H2c, aboveground biomass (**B**) is the predictor). (**C**,**D**) the measured *vs.* predicted belowground biomass outcome from the best models for *Typha* spp. and *S. acutus* respectively. RMSEP is root mean squared error of prediction in g·m^{-2}, while nRMSEP is normalized RMSEP.

4.2.2. Root:Shoot Ratio Hybrid Models

Hybrid models relating spectral reflectance estimates of aboveground plant characteristics to root:shoot ratio were also statistically significant (Table 5; Figure 7). The best models were species specific. For *Typha* spp., % foliar N as a direct single predictor provided the best model (nRMSEP 0.24, explained variance 86 %) (Table 5; Figure 7). For *S. acutus*, combining indirect spectral estimates of belowground biomass (as estimated by spectral estimates of aboveground biomass) and direct spectral estimates of aboveground biomass into a single predictor provided the best model (nRMSEP 0.16, explained variance 80 %) (Table 5; Figure 7).

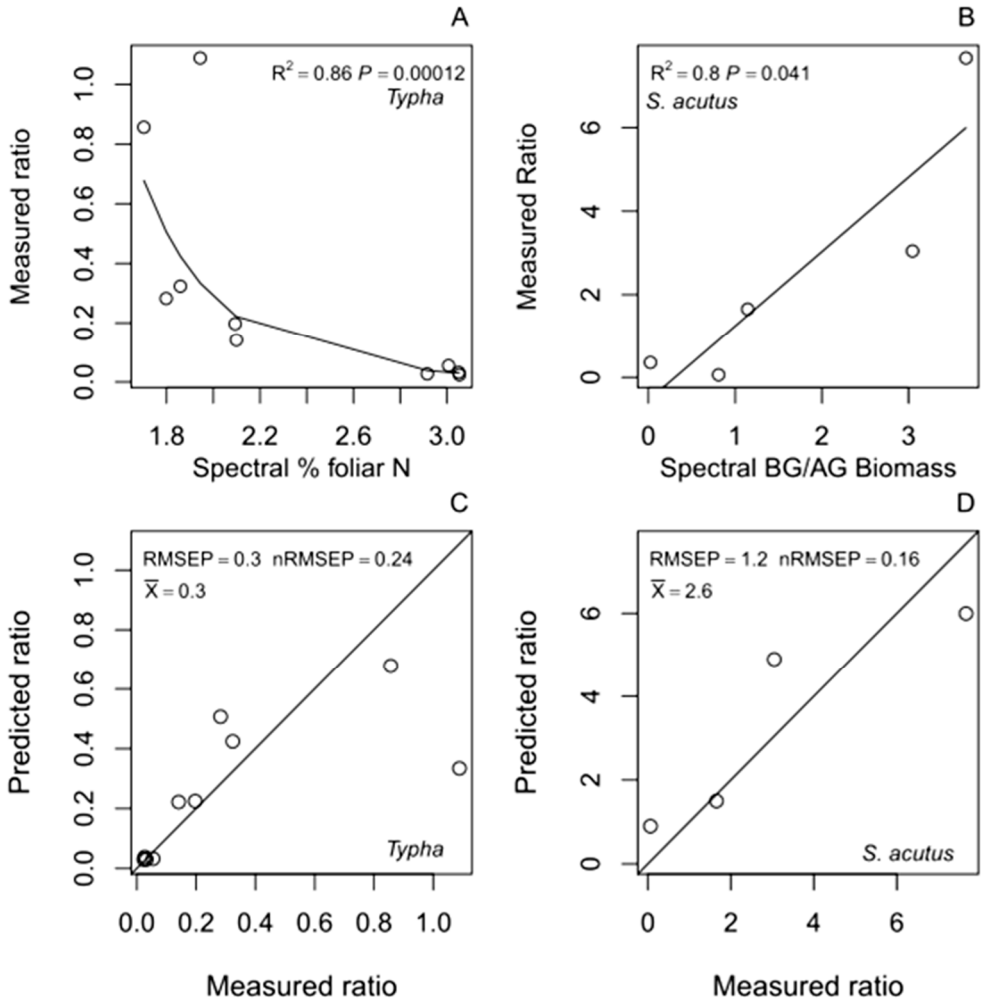

Figure 7. Best root:shoot ratio models for *Typha* (model H4b) (**A**) and *S. acutus* (model H6c) (**B**). The measured *vs.* predicted outcomes from the best models for *Typha* (**C**) and *S. acutus* (**D**). RMSEP is root mean squared error of prediction, nRMSEP is normalized RMSEP.

5. Discussion

We found significant relationships between remote-sensing-based estimates of aboveground plant characteristics, belowground biomass and root:shoot ratios. In our study, field and spectrally estimated % foliar N and aboveground biomass had negative relationships with belowground biomass and biomass allocation in *S. acutus* and *Typha* spp. Field spectroradiometer-based reflectance measurements estimated % foliar N with higher accuracy than multispectral, moderate resolution Landsat 7 satellite data. Nonetheless, Landsat 7 bands overlapped with some hyperspectral wavelengths associated with % foliar N. Also, Landsat 7 estimates of % foliar N were significant for all species, suggesting this public data source might be utilized for estimating coarse variation in canopy N at broad scales. Additionally, inundation had a significant influence on foliar N estimation, and building models of flooded and non-flooded plots separately improved % foliar N estimation. Landsat 7 was particularly useful for *S. acutus* models where 70% of foliar N variation was explained within non-flooded plots. Further, estimates of % foliar N and aboveground biomass from Landsat 7 bands were helpful in estimating belowground biomass and biomass allocation.

5.1. Correlations among Foliar N, Aboveground Biomass and Spectral Reflectance

Remote-sensing studies often estimate foliar N concentration [54,63,64]. In our study, full spectrum field spectroradiometer reflectance data provided the most accurate estimation of % foliar N for *Typha*. Component 1 explained the majority of variation and closely mirrored the spectral

signature of both species. One interpretation is that component 1 estimates the relative cover of the species within the plot. Thus for spectra important to N estimation, we look to Components 2 and 3, where Component 2 explains the most variance. For both species, reflectance data over 500–700 nm, 1000–1200 nm, and greater than 1700 nm were particularly informative. Reflectance over 500–700 nm encompasses peak greenness and the red edge. Reflectance at 550 nm, peak greenness, is associated with chlorophyll [45,65], which contains 6.5% N by weight: 30%–50% of foliar N is within ribulose-1,5-biphosphate carboxylase-oxygenase (rubisco) inside chloroplasts [47]. Chlorophyll and foliar N are thus associated with photosynthesis and plant productivity. Red edge reflectance also has been associated with plant stress and N accumulation [66].

Reducing hyperspectral to multispectral data resulted in some loss of precision. All Landsat 7 bands corresponded to bands with high absolute loadings values from hyperspectral analysis, though not all hyperspectral bands with high absolute loadings values were captured by Landsat measures. Shortwave spectra were important for estimating foliar N and likely corresponded to amide bond vibration within proteins [47] (Figure 4). Improvements in the availability and spatial resolution for full spectrum hyperspectral data may one day allow improved site-wide analysis of % foliar N. Additionally, such hyperspectral data should improve estimates of parameters which rely on foliar N measures, such as belowground biomass.

Water depth influenced spectral reflectance of % foliar N in this study. Water is a strong absorber of light, particularly near infrared reflectance [20]. As a consequence, models of non-flooded plots generally converged with fewer components and explained greater variance than flooded plots. Models of flooded plots also were slightly improved over models of the full dataset, suggesting that flooding doesn't limit the ability to estimate N, but rather that datasets should be stratified by water depth before analysis. For aboveground biomass, stratifying analyses by water depth did not improve performance over the full model, perhaps because fewer samples were available for aboveground biomass models and model subsets could not converge.

Future studies wishing to stratify analysis by water depth can apply the modified normalized difference water index (MNDWI) across study sites to identify flooded pixels [67]. This index relies on the reduction in reflectance in green and mid-range infrared wavelengths in flooded *vs.* non-flooded pixels. MNDWI is better able to distinguish water than metrics derived from red and near infrared spectra, such as the normalized difference vegetation index (NDVI) [67].

5.2. Estimating Trends in Belowground Biomass and Biomass Allocation Ratio Using Multispectral Hybrid Models

In combination with our experimental study, we present a first use of spectral data to indirectly estimate belowground biomass and biomass allocation. This effort links several relationships observed in literature: remote-sensing often estimates aboveground biomass [1,47], and foliar N concentration [54,63,64,68–70], foliar N is linked to environmental N [71–74], and aboveground biomass and environmental N together can help estimate biomass allocation [33,75–77]. Our study starts to link remotely-sensed signals to whole-plant biomass.

Plants in our system appeared to correspond to a balanced growth concept, such that plants had either no relationship or a negative relationship with aboveground biomass and a negative relationship with foliar N, a parameter that might serve as a proxy for plant nutrient status. Past studies suggest plants may increase allocation of photosyntate belowground under nutrient limitation to increase absorptive area for nutrient capture and to increase rhizomatic carbohydrate storage as a buffer against future scarcity [41]. However, we suggest caution before assuming that growth patterns detected across a narrow range of nutrients applies outside the studied range. For example, in the case of *Spartina alterniflora,* the dominant macrophyte within eastern U.S. coastal salt marshes, sometimes this species has followed different patterns under different environmental conditions (e.g., isometric growth *sensu* Gross *et al.* [78] and balanced growth *sensu* Valiela *et al.* [79], Morris *et al.* [80] and Deegan *et al*. [33]). Interestingly, Gross *et al.* [78] observed isometric growth for interior marsh *S. alternifora*, whereas at the channel edge, a location where the majority of nutrient-rich sediments are deposited, *S. alterniflora* did not grow isometrically. Reliably modeling belowground

biomass therefore requires study specific investigations of biomass relationships across site-wide nutrient gradients.

In our study, when foliar N was correlated with belowground biomass, log transformation improved the relationship, such that belowground biomass was very high were foliar N was low. The majority of the error in RMSEP was derived from plots with low N and high belowground biomass, where even logarithmic curves failed to capture the steepness of the relationship among these variables. While patterns of root growth in response to nutrient limitation are complex, a non-linear increase in belowground biomass at low N seems more reasonable than a linear increase [81].

Other factors can influence model estimates as well. We employed a detection limit for response variables in our hybrid models and included only samples with >10 g for belowground biomass, or >0.01 for root:shoot ratio. Early data exploration suggested that these cut-offs were important for improving model outcomes. Such was particularly true for *S. acutus*, a species that was under represented in our study areas. Also, low belowground biomass plots for *S. acutus* mostly were located in the Twitchell west pond, an impoundment that also had tall dead thatch covering 60% of plots, obscuring portions of *S. acutus* stems (Table 1). For *S. acutus*, thatch accumulation over lower portions of vertically oriented conical stems can mask reflectance from live vegetation, increasing signal noise. Excluding these low biomass plots with high thatch cover improved model performance considerably. In addition, multispectral PLS regression can only generate as many latent variables (components) as there are bands, and thus has less capacity to minimize background effects introduced by non-target cover types. Areas with high cover type heterogeneity probably would be better measured by hyperspectral reflectance with fine spectral resolution. Sensors that may work better in heterogeneous sites include AVIRIS, a hyperspectral sensor (400–2500 nm, 4 m to 20 m spatial resolution depending on platform) (aviris.jpl.nasa.gov). However, Landsat, which measures shortwave infrared spectra, is promising for measuring foliar N and whole plant biomass trends, particularly for pixels that have high cover of target response species. Landsat 8 Operational Land Imager, while not available when our study was conducted, also includes two shortwave infrared bands and may be useful for future work. These techniques may have broadest utility within coastal marshes, many of which are dominated by one to a few species (e.g., salt and brackish marshes).

Finally, mixed species models performed poorly compared to species specific models. For situations where all species do not respond similarly to predictor variables, mixed species models may give misleading results [53]. We recommend undertaking species specific investigations before generalizing to mixed species models, to identify potentially confounding correlates.

5.3. Applications of Multispectral Hybrid Modeling of Belowground Biomass and Root:Shoot Ratio

Many models for carbon accounting or for modeling ecosystem transitions may be improved by incorporating spatially explicit variation in productivity. For example, the Marsh Equilibrium Model [82] is a process-based model predicting carbon sequestration and coastal marsh fate with sea level rise. Among other variables, users parameterize this model with a single estimate of aboveground biomass and root:shoot ratio. Other models related to wetland longevity with climate change include the Sea Level Affecting Marshes Model [83], which takes marsh accretion as an input parameter. Currently these models allow only one number to estimate accretion, below and aboveground biomass or root:shoot ratio, which is not as realistic. There have been efforts to make such models more spatially explicit [84,85], but more work remains. Our modeling approach provides another tool to assist with precision forecasting of wetland fates as climate changes and sea levels rise.

Additionally, our approach may advance ecological theories concerning belowground biomass. For example, there is controversy concerning the influence of eutrophication within coastal marshes. Some suggest excess environmental nutrients reduce belowground biomass and accelerate marsh loss [33,75,76,86]. Further, Turner *et al.* [87,88] reasoned that sediment diversions onto marsh surfaces, a common wetland restoration technique, might have unintended consequences when sediments are nutrient rich. Such diversions could reduce belowground biomass and soil stability within coastal marshes, making them vulnerable to hurricane damage. Contrarily, others argue that declining sediment supply is a main threat to coastal wetlands [89,90]. In this view, sediment

diversions increase marsh health by stimulating belowground productivity, adding to soil volume, and increasing marsh accretion [77,89,91]. We do not enter this debate except to suggest that our modeling approach may reduce the cost of estimating correlations among eutrophication, plant uptake as foliar N, and resulting productivity responses, helping to resolve these issues.

6. Conclusions

Hyperspectral and multispectral analysis are promising tools for estimating % foliar N in wetlands and also for indirectly estimating relative measures in belowground biomass and biomass allocation. Species specific investigations of these relationships are necessary to parameterize new modeling efforts at other sites. Currently, measures of variation in belowground biomass are difficult to obtain. However, publically available Landsat data provide global and long-term estimates of landscape change [92]. When properly supported by field and experimental studies, this modeling approach may reduce the time and cost of site and landscape monitoring of belowground biomass and root:shoot ratio. Approaches in this paper can assist with identifying high and low extremes of foliar N and belowground biomass which might be targeted for additional investigations. Our approach may provide best results within low diversity areas with somewhat homogeneous plot cover. Water depth also influences model outcomes and must be accounted for or minimized. As hyperspectral imaging technologies become more widely available, the predictive capacity and applicability of such models also may improve.

Acknowledgements: This research was supported by K. Byrd's NASA New Investigator Program in Earth Sciences Grant Number: NNH10A086I. We thank Susan Stitt and Carol Mladinich, Don Mulcahy, James Bartolome, Lisamarie Windham-Myers, Kyra Engelberg, Caitlyn Chew, Adam McClure and Jenny Palomino for their assistance with equipment, supplies, lab space and field labor. Any use of trade, firm, or product names is for descriptive purposes only and does not imply endorsement by the U.S. Government.

Author Contributions: Byrd wrote the grant that funded the work. Kelly provided infrastructure and logistical support. O'Connell and Byrd collected the data. O'Connell conducted the statistical analysis. All authors contributed to writing the text, editing and reviewing the manuscript.

Conflicts of Interest: The authors declare no conflict of interest.

Abbreviations Used in Text, Tables and Figures

Aboveground biomass (AG biomass); Belowground biomass (BG biomass); Explained variance (EV); Hybrid models (H1.H6); Landsat Ecosystem Disturbance Adaptive Processing System (LEDAPS); Modified Normalized Difference Water Index (MNDWI); Nitrogen (N); Normalized root mean square error of prediction (nRMSEP); Normalized Difference Vegetation Index (NDVI); Partial least squares (PLS); Root mean square error of prediction (RMSEP); Root:shoot ratio (RS); *Schoenoplectus acutus* (*S. acutus*); Spectral models (S1.S3); *Typha* (*T.*).

References

1. Smith, M.-L.; Ollinger, S.V.; Martin, M.E.; Aber, J.D.; Hallett, R.A.; Goodale, C.L. Direct estimation of aboveground forest productivity through hyperspectral remote sensing of canopy nitrogen. *Ecol. Appl.* **2002**, *12*, 1286–1302.
2. Lu, D.S. The potential and challenge of remote sensing-based biomass estimation. *Int. J. Remote Sens.* **2006**, *27*, 1297–1328.
3. Rasse, D.P.; Rumpel, C.; Dignac, M.-F. Is soil carbon mostly root carbon? Mechanisms for a specific stabilisation. *Plant Soil* **2005**, *269*, 341–356.
4. Post, W.M.; Emanuel, W.R.; Zinke, P.J.; Stangenberger, A.G. Soil carbon pools and world life zones. *Nature* **1982**, *298*, 156–159.
5. Moore, P.D. Ecological and hydrological aspects of peat formation. *Geol. Soc. Spec. Publ.* **1987**, *32*, 7–15.
6. Prokopovich, N.P. Subsidence of peat in California and Florida. *Bull. Assoc. Eng. Geol.* **1985**, *22*, 395–420.
7. Bridgham, S.D.; Megonigal, J.P.; Keller, J.K.; Bliss, N.B.; Trettin, C. The carbon balance of North American wetlands. *Wetlands* **2006**, *26*, 889–916.

8. DeLaune, R.D.; Nyman, J.A.; Jr., W.H.P. Peat collapse, ponding and wetland loss in a rapidly submerging coastal marsh. *J. Coast. Res.* **1994**, *10*, 1021–1030.
9. Törnqvist, T.E.; Wallace, D.J.; Storms, J.E.A.; Wallinga, J.; Dam, R.L. van Blaauw, M.; Derksen, M.S.; Klerks, C.J.W.; Meijneken, C.; Snijders, E.M.A. Mississippi Delta subsidence primarily caused by compaction of Holocene strata. *Nat. Geosci.* **2008**, *1*, 173–176.
10. Deverel, S.J.; Leighton, D.A. Historic, recent, and future subside, Sacramento-San Joaquin Delta, CA, USA. *San Franc. Estuary Watershed Sci.* **2010**, *8*, 1-23.
11. Nungesser, M.K. Reading the landscape: Temporal and spatial changes in a patterned peatland. *Wetlands Ecol. Manag.* **2011**, *19*, 475–493.
12. Nyman, J.A.; Delaune, R.D.; Roberts, H.H.; Patrick, W.H. Relationship between vegetation and soil formation in a rapidly submerging coastal marsh. *Mar. Ecol. Prog. Ser.* **1993**, *96*, 269–279.
13. Morris, J.T.; Sundareshwar, P.V.; Nietch, C.T.; Kjerfve, B.; Cahoon, D.R. Responses of coastal wetlands to rising sea level. *Ecology* **2002**, *83*, 2869–2877.
14. Miller, R.L.; Fram, M.; Fujii, R.; Wheeler, G. Subsidence reversal in a re-established wetland in the Sacramento-San Joaquin Delta, CA, USA. *San Franc. Estuary Watershed Sci.* **2008**, *6*, 1-16.
15. Zedler, J.B.; Kercher, S. Wetland resources: Status, trends, ecosystem services, and restorability. *Annu. Rev. Environ. Resour.* **2005**, *30*, 39–74.
16. Benton, A.; Newman, R. Color aerial photography for aquatic plant monitoring. *J. Aquat. Plant Manag.* **1976**, *14*, 14–16.
17. Adam, E.; Mutanga, O.; Rugege, D. Multispectral and hyperspectral remote sensing for identification and mapping of wetland vegetation: A review. *Wetlands Ecol. Manag.* **2010**, *18*, 281–296.
18. Klemas, V. Remote sensing of coastal wetland biomass: An overview. *J. Coast. Res.* **2013**, *290*, 1016–1028.
19. Klemas, V. Remote sensing of emergent and submerged wetlands: An overview. *Int. J. Remote Sens.* **2013**, *34*, 6286–6320.
20. Mishra, D.R.; Cho, H.J.; Ghosh, S.; Fox, A.; Downs, C.; Merani, P.B.T.; Kirui, P.; Jackson, N.; Mishra, S. Post-spill state of the marsh: Remote estimation of the ecological impact of the Gulf of Mexico oil spill on Louisiana Salt Marshes. *Remote Sens. Environ.* **2012**, *118*, 176–185.
21. Byrd, K.B.; O'Connell, J.L.; Di Tommaso, S.; Kelly, M. Evaluation of sensor types and environmental controls on mapping biomass of coastal marsh emergent vegetation. *Remote Sens. Environ.* **2014**, *149*, 166–180.
22. Ramsey, E.W., III; Sapkota, S.K.; Barnes, F.G.; Nelson, G.A. Monitoring the recovery of *Juncus roemerianus* marsh burns with the normalized difference vegetation index and Landsat Thematic Mapper data. *Wetlands Ecol. Manag.* **2002**, *10*, 85–96.
23. Turpie, K.R.; Klemas, V.V.; Byrd, K.B.; Kelly, M.; Jo, Y.-H. Prospective HyspIRI global observations of tidal wetlands. *Remote Sens. Environ.* **2015**, *167*, 206–217.
24. Rundquist, D.C.; Narumalani, S.; Narayanan, R.M. A review of wetlands remote sensing and defining new considerations. *Remote Sens. Rev.* **2001**, *20*, 207–226.
25. Phinn, S.R.; Stow, D.A.; Zedler, J.B. Monitoring wetland habitat restoration in southern California using airborne multi spectral video data. *Restor. Ecol.* **1996**, *4*, 412–422.
26. Phinn, S.R. A framework for selecting appropriate remotely sensed data dimensions for environmental monitoring and management. *Int. J. Remote Sens.* **1998**, *19*, 3457–3463.
27. Kearney, M.S.; Stutzer, D.; Turpie, K.; Stevenson, J.C. The effects of tidal inundation on the reflectance characteristics of coastal marsh vegetation. *J. Coast. Res.* **2009**, *256*, 1177–1186.
28. Turpie, K.R. Explaining the spectral red-edge features of inundated marsh vegetation. *J. Coast. Res.* **2013**, *290*, 1111–1117.
29. Geladi, P.; Kowalski, B.R. Partial least-squares regression: A tutorial. *Anal. Chim. Acta* **1986**, *185*, 1–17.
30. Mevik, B.-H.; Cederkvist, H.R. Mean squared error of prediction (MSEP) estimates for principal component regression (PCR) and partial least squares regression (PLSR). *J. Chemom.* **2004**, *18*, 422–429.
31. Chen, J.; Gu, S.; Shen, M.; Tang, Y.; Matsushita, B. Estimating aboveground biomass of grassland having a high canopy cover: An exploratory analysis of *in situ* hyperspectral data. *Int. J. Remote Sens.* **2009**, *30*, 6497–6517.
32. Mokany, K.; Raison, R.J.; Prokushkin, A.S. Critical analysis of root:shoot ratios in terrestrial biomes. *Glob. Change Biol.* **2006**, *12*, 84–96.
33. Deegan, L.A.; Johnson, D.S.; Warren, R.S.; Peterson, B.J.; Fleeger, J.W.; Fagherazzi, S.; Wollheim, W.M. Coastal eutrophication as a driver of salt marsh loss. *Nature* **2012**, *490*, 388–392.

34. Yu, Q.; Wu, H.; He, N.; Lü, X.; Wang, Z.; Elser, J.J.; Wu, J.; Han, X. Testing the growth rate hypothesis in vascular plants with above- and below-ground biomass. *PLoS ONE* **2012**, *7*, e32162.
35. O'Connell, J.L.; Byrd, K.B.; Kelly, M. Remotely-Sensed indicators of N-related biomass allocation in *Schoenoplectus acutus*. *PLoS ONE* **2014**, *9*, e90870.
36. Cohen, R.A.; Fong, P. Using opportunistic green macroalgae as indicators of nitrogen supply and sources to estuaries. *Ecol. Appl.* **2006**, *16*, 1405–1420.
37. Sheppard, J.K.; Carter, A.B.; McKenzie, L.J.; Pitcher, C.R.; Coles, R.G. Spatial patterns of sub-tidal seagrasses and their tissue nutrients in the Torres Strait, northern Australia: Implications for management. *Cont. Shelf Res.* **2008**, *28*, 2282–2291.
38. Siciliano, D.; Wasson, K.; Potts, D.C.; Olsen, R.C. Evaluating hyperspectral imaging of wetland vegetation as a tool for detecting estuarine nutrient enrichment. *Remote Sens. Environ.* **2008**, *112*, 4020–4033.
39. Suwandana, E.; Kawamura, K.; Sakuno, Y.; Evri, M.; Lesmana, A.H. Hyperspectral reflectance response of seagrass (*Enhalus acoroides*) and brown algae (*Sargassum* sp.) to nutrient enrichment at laboratory scale. *J. Coast. Res.* **2012**, *28*, 956–963.
40. Mozdzer, T.J.; McGlathery, K.J.; Mills, A.L.; Zieman, J.C. Latitudinal variation in the availability and use of dissolved organic nitrogen in Atlantic coast salt marshes. *Ecology* **2014**, *95*, 3293–3303.
41. Kobe, R.K.; Iyer, M.; Walters, M.B. Optimal partitioning theory revisited: Nonstructural carbohydrates dominate root mass responses to nitrogen. *Ecology* **2010**, *91*, 166–179.
42. Mccarthy, M.C.; Enquist, B.J. Consistency between an allometric approach and optimal partitioning theory in global patterns of plant biomass allocation. *Funct. Ecol.* **2007**, *21*, 713–720.
43. Dong, J.; Kaufmann, R.K.; Myneni, R.B.; Tucker, C.J.; Kauppi, P.E.; Liski, J.; Buermann, W.; Alexeyev, V.; Hughes, M.K. Remote sensing estimates of boreal and temperate forest woody biomass: Carbon pools, sources, and sinks. *Remote Sens. Environ.* **2003**, *84*, 393–410.
44. Thenkabail, P.S.; Stucky, N.; Griscom, B.W.; Ashton, M.S.; Diels, J.; van der Meer, B.; Enclona, E. Biomass estimations and carbon stock calculations in the oil palm plantations of African derived savannas using IKONOS data. *Int. J. Remote Sens.* **2004**, *25*, 5447–5472.
45. Townsend, P.A.; Foster, J.R.; Chastain, R.A.; Currie, W.S. Application of imaging spectroscopy to mapping canopy nitrogen in the forests of the central Appalachian Mountains using Hyperion and AVIRIS. *IEEE Trans. Geosci. Remote Sens.* **2003**, *41*, 1347–1354.
46. Martin, M.E.; Plourde, L.C.; Ollinger, S.V.; Smith, M.-L.; McNeil, B.E. A generalizable method for remote sensing of canopy nitrogen across a wide range of forest ecosystems. *Remote Sens. Environ.* **2008**, *112*, 3511–3519.
47. Kokaly, R.F.; Asner, G.P.; Ollinger, S.V.; Martin, M.E.; Wessman, C.A. Characterizing canopy biochemistry from imaging spectroscopy and its application to ecosystem studies. *Remote Sens. Environ.* **2009**, *113* (Suppl. S1), S78–S91.
48. Liu, J.; Pattey, E.; Miller, J.R.; McNairn, H.; Smith, A.; Hu, B. Estimating crop stresses, aboveground dry biomass and yield of corn using multi-temporal optical data combined with a radiation use efficiency model. *Remote Sens. Environ.* **2010**, *114*, 1167–1177.
49. Mezzini, E. New Techniques for the Remote Sensing of Foliar Nitrogen Concentration in Forest Ecosystems. Ph.D. Thesis, University of Bologna, Bologna, Italy, 2013.
50. Phillips, R.L.; Beeri, O.; Liebig, M. Landscape estimation of canopy C:N ratios under variable drought stress in Northern Great Plains rangelands. *J. Geophys. Res.-Biogeosci.* **2006**, *111*, doi:10.1029/2005JG000135.
51. Zhao, C.J.; Liu, L.Y.; Wang, J.H.; Huang, W.J.; Song, X.Y.; Li, C.J. Predicting grain protein content of winter wheat using remote sensing data based on nitrogen status and water stress. *Int. J. Appl. Earth Observ. Geoinf.* **2005**, *7*, 1–9.
52. Curran, P.J. Remote sensing of foliar chemistry. *Remote Sens. Environ.* **1989**, *30*, 271–278.
53. Knyazikhin, Y.; Schull, M.A.; Stenberg, P.; Mõttus, M.; Rautiainen, M.; Yang, Y.; Marshak, A.; Carmona, P.L.; Kaufmann, R.K.; Lewis, P.; *et al*. Hyperspectral remote sensing of foliar nitrogen content. *Proc. Natl. Acad. Sci. USA* **2013**, *110*, E185–E192.
54. Stroppiana, D.; Fava, F.; Baschetti, M.; Brivio, P.A. Estimation of nitrogen content in crops and pastures using hyperspectral vegetation indices. In *Hyperspectral Remote Sensing of Vegetation*; Thenkabail, P.S., Lyon, J.G., Huete, A., Eds.; CRC Press: Boca Raton, FL, USA, 2012; pp. 245–262.
55. Deverel, S.J.; Rojstaczer, S. Subsidence of agricultural lands in the Sacramento-San Joaquin Delta, California: Role of aqueous and gaseous carbon fluxes. *Water Resour. Res.* **1996**, *32*, 2359–2367.

56. McKee, K.L. Biophysical controls on accretion and elevation change in Caribbean mangrove ecosystems. *Estuar. Coast. Shelf Sci.* **2011**, *91*, 475–483.
57. Neill, C. Comparison of soil coring and ingrowth methods for measuring belowground production. *Ecology* **1992**, *73*, 1918–1921.
58. Hargis, T.G.; Twilley, R.R. Improved coring device for measuring soil bulk density in a Louisiana deltaic marsh. *J. Sediment. Res.* **1994**, *64*, 681–683.
59. Miller, R.L.; Fujii, R. Plant community, primary productivity, and environmental conditions following wetland re-establishment in the Sacramento-San Joaquin Delta, California. *Wetlands Ecol. Manag.* **2010**, *18*, 1–16.
60. Masek, J.G.; Vermote, E.F.; Saleous, N.; Wolfe, R.; Hall, F.G.; Huemmrich, F.; Gao, F.; Kutler, J.; Lim, T.K. *LEDAPS Landsat Calibration, Reflectance, Atmospheric Correction Preprocessing Code*; Oak Ridge National Laboratory Distributed Active: Oak Ridge, TN, USA; 2012. http://dx.doi.org/10.3334/ORNLDAAC/1080.
61. Mevik, B.-H.; Wehrens, R. The PLS package: Principle component and partial least-squares regression in R. *J. Stat. Softw.* **2007**, *18*, 1–24.
62. Efron, B. Better bootstrap confidence intervals. *J. Am. Stat. Assoc.* **1987**, *82*, 171–185.
63. Abdel-Rahman, E.M.; Ahmed, F.B.; Ismail, R. Random forest regression and spectral band selection for estimating sugarcane leaf nitrogen concentration using EO-1 Hyperion hyperspectral data. *Int. J. Remote Sens.* **2013**, *34*, 712–728.
64. Tian, Y.C.; Yao, X.; Yang, J.; Cao, W.X.; Hannaway, D.B.; Zhu, Y. Assessing newly developed and published vegetation indices for estimating rice leaf nitrogen concentration with ground- and space-based hyperspectral reflectance. *Field Crops Res.* **2011**, *120*, 299–310.
65. Thenkabail, P.S.; Smith, R.B.; De-Pauw, E. Evaluation of narrowband and broadband vegetation indices for determining optimal hyperspectral wavebands for agricultural crop characteristics. *Photogramm. Eng. Remote Sens.* **2002**, *68*, 607–621.
66. Thenkabail, P.S.; Lyon, J.G.; Huete, A. Advances in hyperspectral remote sensing of vegetation and agricultural croplands. In *Hyperspectral Remote Sensing of Vegetation*; Thenkabail, P.S., Lyon, J.G., Huete, A., Eds.; Taylor and Francis Group: Boca Raton, FL, USA, 2012; pp. 28–29.
67. Xu, H. Modification of normalised difference water index (NDWI) to enhance open water features in remotely sensed imagery. *Int. J. Remote Sens.* **2006**, *27*, 3025–3033.
68. Stroppiana, D.; Boschetti, M.; Brivio, P.A.; Bacchi, S. Plant nitrogen concentration in paddy rice from field canopy hyperspectral radiometry. *Field Crops Res.* **2009**, *111*, 119–129.
69. Ryu, C.; Suguri, M.; Umeda, M. Model for predicting the nitrogen content of rice at panicle initiation stage using data from airborne hyperspectral remote sensing. *Biosyst. Eng.* **2009**, *104*, 465–475.
70. Mokhele, T.A.; Ahmed, F.B. Estimation of leaf nitrogen and silicon using hyperspectral remote sensing. *J. Appl. Remote Sens.* **2010**, *4*, 043560-043560-18.
71. Sartoris, J.J.; Thullen, J.S.; Barber, L.B.; Salas, D.E. Investigation of nitrogen transformations in a southern California constructed wastewater treatment wetland. *Ecol. Eng.* **1999**, *14*, 49–65.
72. Bedford, B.L.; Walbridge, M.R.; Aldous, A. Patterns in nutrient availability and plant diversity of temperate North American wetlands. *Ecology* **1999**, *80*, 2151–2169.
73. Kao, J.T.; Titus, J.E.; Zhu, W.-X. Differential nitrogen and phosphorus retention by five wetland plant species. *Wetlands* **2003**, *23*, 979–987.
74. Larkin, D.J.; Lishawa, S.C.; Tuchman, N.C. Appropriation of nitrogen by the invasive cattail *Typha × glauca*. *Aquat. Bot.* **2012**, *100*, 62–66.
75. Darby, F.A.; Turner, R.E. Below- and aboveground biomass of *Spartina alterniflora*: Response to nutrient addition in a Louisiana salt marsh. *Estuar. Coasts* **2008**, *31*, 326–334.
76. Turner, R.E.; Howes, B.L.; Teal, J.M.; Milan, C.S.; Swenson, E.M.; Toner, D.D.G. Salt marshes and eutrophication: An unsustainable outcome. *Limnol. Oceanogr.* **2009**, *54*, 1634–1642.
77. Morris, J.T.; Shaffer, G.P.; Nyman, J.A. Brinson review: Perspectives on the influence of nutrients on the sustainability of coastal. *Wetlands* **2013**, *33*, 975–988.
78. Gross, M.F.; Hardisky, M.A.; Wolf, P.L.; Klemas, V. Relationship between aboveground and belowground biomass of *Spartina alterniflora* (smooth cordgrass). *Estuaries* **1991**, *14*, 180–191.
79. Valiela, I.; Teal, J.M.; Persson, N.Y. Production and dynamics of experimentally enriched salt marsh vegetation: Belowground biomass. *Limnol. Oceanogr.* **1976**, *21*, 245–252.
80. Morris, J. A model of growth responses by *Spartina alterniflora* to nitrogen limitation. *J. Ecol.* **1982**, *70*, 25–42.

81. Dunbabin, V.; Postma, J.; Schnepf, A.; Pagès, L.; Javaux, M.; Wu, L.; Leitner, D.; Chen, Y.; Rengel, Z.; Diggle, A. Modelling root-soil interactions using three–dimensional models of root growth, architecture and function. *Plant Soil* **2013**, *372*, 93–124.
82. Morris, J.T. The Marsh Equilibrium Model MEM 3.4. Available online: http://jellyfish.geol.sc.edu/model/marsh/mem.asp (accessed on 3 November 2014).
83. Warren Pinnacle Consulting, Inc. SLAMM: Sea Level Affecting Marshes Model. Available online: http://www.warrenpinnacle.com/prof/SLAMM/ (accessed on 4 November 2013).
84. Schile, L.M.; Callaway, J.C.; Morris, J.T.; Stralberg, D.; Parker, V.T.; Kelly, M. Modeling tidal marsh distribution with sea-level rise: Evaluating the role of vegetation, sediment, and upland habitat in marsh resiliency. *PLoS ONE* **2014**, *9*, e88760.
85. Stralberg, D.; Brennan, M.; Callaway, J.C.; Wood, J.K.; Schile, L.M.; Jongsomjit, D.; Kelly, M.; Parker, V.T.; Crooks, S. Evaluating tidal marsh sustainability in the face of sea-level rise: A hybrid modeling approach applied to San Francisco Bay. *PLoS ONE* **2011**, *6*, e27388.
86. Darby, F.A.; Turner, R.E. Effects of eutrophication on salt marsh root and rhizome biomass accumulation. *Mar. Ecol. Prog. Ser.* **2008**, *363*, 63–70.
87. Turner, R.E. Wetland loss in the northern Gulf of Mexico: Multiple working hypotheses. *Estuaries* **1997**, *20*, 1–13.
88. Turner, R.E. Coastal wetland subsidence arising from local hydrologic manipulations. *Estuaries* **2004**, *27*, 265–272.
89. Day, J.; Britsch, L.; Hawes, S.; Shaffer, G.; Reed, D.; Cahoon, D. Pattern and process of land loss in the Mississippi Delta: A Spatial and temporal analysis of wetland habitat change. *Estuar. Coasts* **2000**, *23*, 425–438.
90. Weston, N.B. Declining sediments and rising seas: An unfortunate convergence for tidal wetlands. *Estuar. Coasts* **2014**, doi:10.1007/s12237-013-9654-8.
91. Lane, R.R.; Day, J.W.; Thibodeaux, B. Water quality analysis of a freshwater diversion at Caernarvon, Louisiana. *Estuaries* **1999**, *22*, 327–336.
92. Wulder, M.A.; Masek, J.G.; Cohen, W.B.; Loveland, T.R.; Woodcock, C.E. Opening the archive: How free data has enabled the science and monitoring promise of Landsat. *Remote Sens. Environ.* **2012**, *122*, 2–10.